Utility of radiosonde wind data in representing climatological variations of tropospheric temperature and baroclinicity in the western tropical Pacific

Submitted to Journal of Climate

June 1, 2006

Resubmitted December 8, 2006

Robert J. Allen and Steven C. Sherwood

Dept. of Geology and Geophysics

Yale University, New Haven, CT

Corresponding author address:

Robert Allen, Yale University, New Haven, CT 06520-8109 (robert.allen@yale.edu)

Ph#: 203-432-9808; Fax#: 203-432-3134

Abstract

The utility of the thermal wind equation (TWE) in relating tropospheric (850 to 300 hPa) wind and temperature on climatological time scales is assessed, based on data from 59 radiosonde stations in the western tropical Pacific during 1979-2004. Observed long-term mean and seasonal variations closely obey geostrophic balance; incorporating additional (ageostrophic) terms yields negligible improvement. We conclude that observed winds offer a useful constraint on the horizontal structure of monthly and longer temperature variations (although the reverse is not true close to the equator where $f \rightarrow 0$). This conclusion is also supported by general circulation model output.

Wind data show a slowing of the midlatitude jets in the maritime continent region since 1979, indicating that tropical thicknesses and temperature have increased less than those poleward of 25°N/S. This pattern is consistent with Microwave Sounding Unit temperature trends in the region, but is exaggerated south of the equator in trends obtained directly from the temperature data. The latter are however sensitive to which stations are used and how the data are averaged, and the discrepancy is fairly small in a homogenized climatology from the Hadley Centre (HadAT). The discrepancy is most easily explained by spurious cooling at stations in the near equatorial western Pacific. These results support the use of the wind field as a way of overcoming heterogeneities in the temperature records in the monitoring of climate change patterns.

1. Introduction

Variations in the horizontal and vertical temperature structure of the atmosphere are an important diagnostic for climate change attribution and detection (e.g. Tett et al., 2002). Most studies have focused on the vertical profile of temperature change through analysis of radiosonde temperature or satellite data. Since the satellite era, radiosondes and the University of Alabama at Huntsville (UAH) satellite show surface warming which exceeds that in the troposphere, in particular for the tropics (Gaffen et al., 2000; Lanzante et al. 2003b; Thorne et al., 2005; Brown et al. 2000; Karl et al., 2006; Christy et al., 2003). Climate model simulations, as well as the Remote Sensing Systems (RSS) and University of Maryland (UMd) satellite data, predict maximum warming in the tropical middle and upper troposphere (Tett et al., 2002; Karl et al., 2006; Mears et al., 2003; Vinnikov et al., 2006; Fu and Johanson, 2005, Fu et al., 2004). This inconsistency between temperature trends at the surface and troposphere has raised concern about the ability of climate models to predict climate change, and the homogeneity of satellite and (especially) radiosonde temperature data.

Several authors have documented non-climatic inhomogeneities (i.e. time varying systematic biases) in the radiosonde temperature archive (Gaffen, 1994; Eskridge et al., 1995; Lanzante et al., 2003a; Free et al., 2002; Sherwood et al., 2005; Free et al., 2005; Randel and Wu, 2006). Examples include changes in radiosonde type related to changes in temperature sensor or its exposure; changes in observation time; and station relocations. These changes can lead to significant discontinuities in the temperature record from several tenths to as high a several degrees Celsius, which are as large as the temperature trend of a few tenths of a degree per decade over the latter half of the 20th

century (Gaffen, 1994; Parker and Cox, 1995).

Analysis of the wind field offers an alternative approach to the monitoring of climate change. For example, Pielke et al. (2001) analyzed trends in the 200 hPa winds (based on NCEP Reanalysis data), looking for changes in the atmospheric circulation. They showed that since 1958, the 200 hPa westerly flow has increased at most higher latitudes. These changes in the flow can be linked to corresponding changes in the thermal structure through the thermal wind equation (TWE—see Section 3 below) thus indicating an increased equator-to-pole temperature gradient. This conclusion however depends on (1) errors in the wind field being sufficiently small and independent of those in temperature, and (2) climate changes being approximately geostrophically balanced. The former condition is unlikely to hold in reanalyses. For example, Trenberth and Smith (2005) showed that the conservation of mass is violated in such reanalyses, which imply likely momentum budget problems as well. The introduction of satellite data in 1979 also caused spurious shifts in temperature and (presumably) winds (e.g. Pawson and Fiorino, 1999). Others have also noted the impact that changes in the observing system and data assimilation procedures have on the NCEP reanalysis data, specially in the context of trend evaluation (e.g. Kinter et al., 2004).

There have been few studies testing the validity of the geostrophic approximation for climate changes. In fact, most initial long-term wind analyses have simply assumed geostrophy (mostly due to the greater availability of height and pressure data) and presented geostrophic as opposed to measured winds (e.g. van Loon, 1972). Those studies that have investigated geostrophy have been short-term, either looking at a few case studies or at most, a few years. In most of these short-term studies, geostrophic and observed wind speeds differed by 25-40% (e.g. Wu and Jehn, 1972).

One of the few studies that have investigated the climatological accuracy of the geostrophic wind has been by Mori (1988). Using Japanese radiosonde data from 1961-1980, the mean geostrophic winds at 850 hPa (based on observed heights) agreed closely with the observed 850 hPa winds in both magnitude and direction. At 1000 hPa, however, the geostrophic approximation broke down due to surface drag, as would be expected. Mori (1988) also found that the thermal wind estimated from the geostrophic winds at 850 and 1000 hPa agree well with that estimated from the mean horizontal temperature gradient on the 900 hPa surface.

Similarly, Randel (1987) looked at the climatological (1979-85) winter zonal mean zonal geostrophic wind and compares it to higher order relationships between the wind and geopotential, focusing on the stratosphere. Balance zonal mean zonal winds yielded the best estimates (in particular in the stratosphere), although the gradient and geostrophic winds were nearly as accurate in the troposphere. Comparison of these different wind estimates was also made for a general circulation model (GCM) simulation (over 90 days) of the Northern Hemisphere (NH) winter troposphere and stratosphere. Model winds also showed that the balance method is the more accurate technique for local winds in the stratosphere. All three methods, however, yielded approximately the same results in the troposphere, with mean errors between 0-2 ms^{-1} (larger error at lower latitude). This was essentially the same result that Boville (1987) reached. The winter NH 90-day zonal mean zonal winds based on the model and geostrophic balance showed reasonably good agreement in the troposphere, even at lower latitudes (10-20°N). The error was small in the extratropical troposphere (0-2 ms^{-1}), but became quite large in the stratosphere. Although these geostrophic analyses focused on the extratropics, a recent result of the East Pacific Investigation of Climate Processes in the Coupled Ocean-

Atmosphere System 2001 (EPIC2001) (Raymond et al., 2004) found geostrophic winds in close agreement to the observed winds, even at low latitudes (8°-12°N).

Like the radiosonde temperature record, inhomogeneities exist in the wind record, primarily the result of changes in wind observing techniques and procedures. For example, wind measuring techniques used by the Bureau of Meteorology in Australia include (in approximate chronological order) 1. manually operated theodolite and pilot balloon; 2. Metox radio positioning theodolite; 3. Omega navigational network; 4. wind-finding radar; and 5. Global Positioning System (GPS) (Michael Joyce, Australian Bureau of Meteorology, Personal Communication). Unlike the situation with temperature, previous studies have not ascertained whether such changes have caused significant time-varying biases in the radiosonde wind data.

This paper explores the utility of using the (radiosonde) wind field as an indicator of climate change. Specifically, we investigate how well geostrophy applies on climatological time scales, focusing on the thermal wind relation between 850 and 300 hPa. Section 2 describes the data used and the study area investigated. Section 3 outlines the procedure used to estimate baroclinicty and depth-averaged temperature ($\bar{T}$) from the wind field. Section 4 presents the results, including the accuracy of the TWE, time series of wind-estimated baroclinicty, zonal trends of wind-estimated $\bar{T}$, and a comparison to HadAT (Thorne et al., 2005), satellite and climate model temperature trends. A summary and concluding remarks are presented in section 5.

2. Data and Study Area

Radiosonde data comes from the Integrated Global Radiosonde Archive (IGRA) (Durre

et al., 2006). Figure 1 shows the location of the study area, bounded by the rectangle defined by 32.5°S ϕ 32.5°N and 95°E λ 175°E, and the location of the 59 radiosondes used in the analysis. Nine of the 59 stations are located just outside the rectangle, less than a half grid point from the boundary of the study area (i.e. < 2.5° latitude or < 5° longitude). These stations are included to aid data interpolation within the rectangle, and because they would be part of the study area based on HadAT. The western tropical Pacific was chosen because the density of radiosonde data is relatively high and the discrepancy between surface and tropospheric temperature trends is large.

The final set of 59 radiosondes (listed in the Appendix) was chosen based on criteria similar to those employed by Thorne et al. (2005). To calculate a monthly value (e.g. thickness or wind shear), we required at least 12 launches with good wind and height data. Soundings with only one of these two quantities were omitted and only 0000 UTC (morning) data were used because of a general lack of 1200 UTC data in the study area. To calculate a seasonal value, we required at least two of the three monthly values, and for an annual average we required all four valid seasons. This resulted in a (station) median number of omitted years equal to two and median percentage of monthly values among good years of 99.6%. Finally, to minimize bias associated with trend estimation, each station needed at least five annual averages in the first and last decade.

In addition to the radiosonde data, we used the archive of coupled atmosphere-ocean GCM data organized by the Program for Climate Model Diagnosis and Intercomparison (PCMDI) for the Fourth Assessment Report (AR4) of the Intergovernmental Panel on Climate Change (IPCC). From 1979-1999, data from the 20th Century Climate Change experiment (20CEN) was used; from 2000-2004 data from the Special Report on Emission Scenarios (SRES) A1B or the Committed Climate

Change experiment (COMMIT) were used. The 5 models listed in Table 1 were chosen because they contained multiple realizations for the 3 experiments considered.

3. Methodology

a) The momentum budget and wind-temperature approximations

Neglect of friction and inertial (acceleration) terms in the equation of motion yields the geostrophic wind. Above the boundary layer, friction should always be small but inertial terms may not be. Retaining the inertial terms, but not the friction term, results in the gradient-wind balance. We calculated gradient winds according to Endlich (1961) and Patoux and Brown (2002) to determine if this is an improvement upon geostrophic winds.

Assuming geostrophic and hydrostatic balance, the thermal wind equation (TWE) relates the vertical wind shear to the horizontal gradient of temperature. Integration of the east-west component of the TWE, for a layer bounded by two isobaric surfaces, yields a relationship between the meridional gradient of the height difference between the top and bottom of the layer (Z), and the corresponding difference between the westerly geostrophic wind shear (S)

$$\frac{dZ}{dy} = -\frac{f}{g_o} S \ , \qquad (1)$$

where f is the Coriolis parameter and go is a constant related to gravity (= 9.8 ms^{-2}). An equivalent equation to (1) holds for the perpendicular, north-south direction. Thickness, Z, and layer mean virtual temperature ($\bar{T}_v$) are related via the hypsometric equation

(HE). Because radiosonde geopotential heights are calculated based on the HE, z is dependent on temperature (FCM-H3, 1997). Substituting the HE into (1) yields

$$\frac{d\bar{T}_v}{dy} = -\frac{f}{R_d}\left[\ln\left(\frac{p_o}{p_1}\right)\right]^{-1} S \ , \quad (2)$$

where R_d is the gas constant for dry air and $p_o > p_1$. Equation (2) states that as the north-south temperature gradient decreases (increases), the vertical westerly shear of the geostrophic wind also decreases (increases). A decrease in upper level (or increase in lower level) wind speeds would be expected anywhere the usual equator-to-pole temperature gradient became weaker. Although $\bar{T}_v$ is also a weak function of moisture, such moisture dependence has been neglected in this study because observed moisture trends based are sufficiently small at ~1-3% decade^{-1} (e.g. Wentz and Schabel, 2000; Trenberth et al., 2005). Such a moisture change in the tropics implies a trend of virtual 850-300 hPa temperature that is about 20 times smaller than the observed temperature trend (Elliot et al., 1994).

In addition to thermal wind balance, higher order relationships between the wind and geopotential (temperature) field exist. The full divergence equation (DE), obtained by operating on the equation of motion with the divergence operator, relates the geopotential field to the horizontal wind field and terms involving the divergence, its temporal rate of change and the vertical velocity. For large-scale motions above the planetary boundary layer, the twisting, frictional and divergence terms can be neglected, yielding the balance equation (BE) (Fankhauser, 1974; Randel, 1987). To determine if

the BE is an improvement upon the TWE, the BE is solved for z (monthly means), based on the observed wind field, using the successive approximation relaxation method (Haltiner & Williams, 1980). Boundary conditions are assumed to be geostrophic.

b) Interpolation procedures

To examine the validity of the geostrophic approximation and its utility for constraining temperatures, we compare wind, baroclinicity (meridional gradient of tropospheric thickness) and temperature estimates. We focus mainly (but not exclusively) on meridional gradients.

Monthly mean geostrophic winds were calculated according to the finite difference approximations, given the distribution of geopotential height z at grid points on a constant pressure surface. The monthly mean height field is obtained by spatially interpolating z at individual stations (which will be discussed in more detail below). Monthly mean gradient winds were calculated similarly, using the finite difference approximation of the trajectory curvature parameter and the monthly mean height field.

To get the meridional gradient of 850-300 hPa thickness Z from winds using (1), each station's annual monthly mean zonal wind shear S across this layer is interpolated onto a regularly spaced grid (10° longitude by 5° latitude) using anisotropic ordinary kriging (Isaaks and Srivastava, 1989; Sherwood, 2000a,b). Changing the grid resolution yielded negligible differences. Parameters of the kriging procedure—such as the range and nugget—are optimized using a jackknife procedure. For example, the (station and annual average) RMS error of S is minimized (equal to 2.8 m/s) for a longitudinal range of 12250 km and a latitudinal range of 4250 km. At each grid point (x,y), the kriged S is

substituted into (4) and an estimate $\hat{Z}_y$ of the meridional gradient of Z is thereby obtained. Monthly error estimates of $\hat{Z}_y$ at each grid point are obtained through use of the TWE and ordinary kriging standard deviation (Isaaks and Srivastava, 1989) of S according to

$$Err\left(\hat{Z}_y(x, y, Y, M)\right) = \left| -\frac{f s_S}{g_o} \right| ,$$

(3)

where x is the grid point longitude, y the latitude, Y is the year, M is the month and s_S is the uncertainty in the interpolated value of S at that point according to the kriging model. We also calculate $\hat{Z}_y$ at each station directly from the station's own data, but instead of using s_S , we obtain those uncertainties directly from the standard error of S at the station

$$Err\left(\hat{Z}_y(st[j], Y, M)\right) = \left| -\frac{f}{g_o} \frac{2 s_S'}{\sqrt{n-1}} \right| ,$$

(4)

where n is the number of valid days in the month, st[j] is the station index and s_S' is the standard deviation of S at a station.

Similarly, the observed thicknesses Z are mapped onto the same grid by kriging the station values. A jackknife procedure is again used to estimate optimum thickness

kriging parameters. We find that the (station and annual average) RMS error of Z is minimized (19.2 m) with a longitudinal range of 15000 km and a latitudinal range of 6000 km. Each of these ranges is larger than the corresponding one for S, consistent with the fact that Z is proportional to the integral of S and is therefore smoother. Finite differences are then used to estimate the meridional gradient of Z from neighboring points on the grid (Z_y). The uncertainty of Z_y is estimated as

$$Err\left(Z_y(x, y, Y, M)\right) = \frac{s_Z}{r_y}, \quad (5)$$

where r_y is the range parameter in the latitudinal direction and s_Z is again the kriging error. A similar procedure is followed for Z_x .

4. Results

a) Wind field analysis

We first considered agreement between annual mean winds at individual stations and those estimated form the height field. The latter become badly behaved near the equator but we have few stations there. We compared accuracy of different methods by considering the median absolute error (MedAE) so as to minimize sensitivity to this problem. The resulting error was 2.34 ms^{-1} for geostrophic and 2.38 ms^{-1} for gradient wind. This error is comparable to those between geostrophic and model winds in the troposphere at lower latitudes found by Randel (1987) and Boville (1987). Lower errors

generally occur in the winter hemisphere, when winds are generally faster (in better agreement with the prior studies). Lower errors also occur farther from the boundary layer, between 500 and 300 hPa, consistent with Mori (1988). This is likely due to reduced friction aloft. In principle, the gradient wind should be closer to the truth than the geostrophic wind, but this did not prove to be the case in practice. We estimated that the inertial term was typically less than 10% of the geostrophic terms and is noisily estimated since it depends on the curvature of the height contours. This noise appears to have outweighed its small benefit. Fortunately, simple geostrophic balance seems to be quite good an annual time scales, so more complicated formulations appear unnecessary. This also implies that eddy momentum flux divergence is relatively small.

b) Baroclinicity estimates using the TWE

We next compared estimates of baroclinicity based on observed winds ($\hat{Z}_y$) and temperatures (Z_y). The correspondence for long-term means at individual stations is shown in Figure 2a. Most points fall on or very near the 1:1 line. The absolute accuracy is slightly better in the Northern Hemisphere (NH), where the RMS error is 1.86×10^{-5} (10^{-5} is approximately equivalent to 1 m height change per degree latitude), compared to 2.06×10^{-5} in the Southern Hemisphere (SH). For both hemispheres, the median absolute percent error (MAPE) (median of $|Z_y - \hat{Z}_y|$ relative to median of $|Z_y|$) is 12.8%, which corresponds to a RMS error of 1.94×10^{-5}.

We have relatively few stations very close to the equator, where geostrophic balance is most suspect. Figure 2b, based on the ensemble mean of ECHAM5/MPI-OM for grid points between 10°N and 10°S, shows that Equation (1) is robust even at low

latitudes (RMS error of 0.17×10^{-5}) according to models based on the full momentum equation. The constraint that wind-estimated thickness gradients → 0 at the equator based on (1) appears to adequately represent the actual thickness gradients. Furthermore, the model's RMS error based on all grid points within the domain (32.5°N to 32.5°S) is 1.18×10^{-5} (MAPE of 7.7%), both slightly lower than the corresponding radiosonde estimates from Fig. 2a.

Figure 3a shows the spatial distribution of the long-term mean meridional thickness gradient. Note that due to a sign convention, contours in the Northern Hemisphere are negative, while those in the Southern Hemisphere are positive. Values range in magnitude from 0 near the equator to 20×10^{-5} near 30°N and 30° S. This is consistent with maximum (minimum) baroclinicity in mid-latitude (equatorial) regions. Throughout the domain, contours of $\hat{Z}_y$ and Z_y show close agreement.

The correspondence between $\hat{Z}_y$ and Z_y appears especially strong in the long-term zonal mean (Figure 3b). The largest disagreement between $\hat{Z}_y$ and Z_y is at most 3×10^{-5}, where $|Z_y| > |\hat{Z}_y|$, and occurs in the subtropics of both hemispheres. Restricting the zonal mean calculation at each latitude to those longitudes with smaller interpolation errors (i.e. omitting fringe areas where extrapolation was necessary) yielded negligible improvement (not shown).

Figure 4a illustrates the ability of the TWE to capture the seasonal variation of baroclinicity. Here, seasonal baroclinic variability for both hemispheres is defined as the difference between December, January, February (DJF) and June, July, August (JJA). Again, there is good correspondence between Z_y and $\hat{Z}_y$. Both show a predominance of negative contours, consistent with greater baroclinicity during winter (i.e. larger

positive (negative) wintertime versus summertime meridional thickness gradient in the SH (NH)). The best agreement is in the tropics and in the Southern Hemisphere where both methods possess minima less than -15×10^{-5} over the Australian continent. North of 20°N, Z_y and $\hat{Z}_y$ diverge as shown in Figure 4b, reaching a maximum difference of nearly 10×10^{-5} at 32.5°N. This difference mostly comes from inland China, where few stations are located and where nearby orography reaches above 850 hPa possibly introducing significant momentum sources.

Time series of Z_y, $\hat{Z}_y$, and $Z_y - \hat{Z}_y$, by 10° latitude bands, are shown in Figure 5 and the corresponding linear trends over the period and their significance are given in Table 2. An annual average meridional thickness gradient is obtained by an unweighted average of Z_y at all grid points within each latitude band. The linear trends for most latitude bands are statistically significant, especially in the SH. Latitude bands 0-10°S, 10-20°S and 0-30°S show a decrease in meridional thickness gradient (toward less positive values) over the satellite era based on both temperature and winds, significant at 95% level (except $\hat{Z}_y$ between 0-30°S). The trend of the difference ($Z_y - \hat{Z}_y$) series for these latitude bands is also negative (and significant at 99% level), indicating a significantly larger decreasing trend of Z_y, as opposed to $\hat{Z}_y$. The only SH latitude bands having a positive meridional thickness gradient trend is 20-30°S (based on temperature) although this is not significant at the 90% level. These results imply that equatorial thicknesses have decreased relative to those in the southern subtropics and mid-latitudes, and hence, the equator to pole temperature gradient ($\overline{T}_y$) has become weaker. This weakening is more pronounced in observed temperatures than winds.

The latitude bands in the NH exhibit predominantly positive trends (toward less

negative values) over the period, although only two are significant. This is consistent with the predominance of negative trends in the SH and suggests a similar weakening $\bar{T}_y$ in the NH. Similar to the SH analysis, this weakening gradient is most pronounced in the temperature-based estimates, as opposed to those based on wind. Latitude bands 10-20°N, 20-30°N and 0-30°N all show an increase in meridional thickness gradient. The only negative trend (although not significant at the 90% level) is for 0-10°N based on Z_y. As was the case for the SH, there are significant trends in the NH Z_y - $\hat{Z}_y$ difference time series. For all latitude bands (except 0-10°N), the trend of Z_y is larger than the corresponding trend of $\hat{Z}_y$.

Table 2 also lists the correlation between Z_y and $\hat{Z}_y$ for each latitude band. All correlations are significant at the 99% level, except those for 0-10°N and 20-30°S, which are significant at the 90% level. Thus suggests similar interannual variations between Z_y and $\hat{Z}_y$, even at lower latitudes.

c) Baroclinicity and depth-averaged temperature trends

Figure 6a shows the zonal mean trend of the two baroclinicity estimates. For each baroclinicity estimate, three different spatial interpolation/gridding methods are shown. These include kriging of each station's annual monthly mean thickness or wind shear, followed by estimation of the corresponding meridional thickness gradient at each grid point. A linear trend is then fit to each grid point's annual mean time series and the corresponding 1-σ uncertainty (standard error) of the trend is estimated (Wilks, 1995). The zonal mean trend and corresponding 1-σ uncertainty is then computed by averaging

these estimates across longitude. This was the procedure outlined in the methodology section and will be referred to as the "standard" method. Alternatively, the wind and temperature-based meridional thickness gradient trends can be estimated at each station based on that station's annual mean S and Z time series, respectively. This station specific trend estimate is subsequently kriged so that a trend is estimated for all grid points. Equation (2) is used to convert the wind shear based trend to a corresponding meridional thickness gradient trend; finite differencing is used to convert the temperature-based trend to a corresponding meridional thickness gradient trend. A zonal mean trend can then be calculated. This interpolation method will be referred to as the "trend-mapping" method (Sherwood, 2000a). The third and final interpolation method is similar to that used in Thorne et al. (2005) and will be referred to as the "binning" method. Each station's annual monthly mean Z_y and $\hat{Z}_y$, as estimated from the standard method, is simply assigned to that station's nearest grid point (with no interpolation). When more than one station has the same closest grid point, that grid point's annual value is estimated as the average of the available station values (many grid points will contain no data). A zonal mean trend and its uncertainty are then estimated.

The same general pattern emerges from both the wind and temperature-based thickness gradients. In the SH extra tropics, between 32.5°S and 25°S, the Z_y trend is positive, indicating a strengthening $\bar{T}_y$. Throughout a large area encompassing the SH subtropics and tropics, between 25°S to 0°, the Z_y trend is negative (weakening $\bar{T}_y$). Based on the observed thickness, this negative trend extends slightly farther north, up to 5°N. From 0° (5° based on the observed Z) to 32.5°N, the trend is positive, indicating a weakening $\bar{T}_y$. Overlaid on this general picture, however, are some notable differences

between the wind and temperature derived thickness gradients.

Based on the zonal winds (and the standard interpolation method), the decadal trend of $\hat{Z}_y$ ranges from +0.10x10^{-5} decade^{-1} near 10-15°N to –0.25x10^{-5} decade^{-1} at 17°S. The location of this minimum and maximum are generally consistent for the three spatial interpolation methods, although the binning method's minimum and maximum are slightly larger and offset toward higher latitudes. The winds estimates are nearly symmetric across the equator, with a weakening equator to pole temperature gradient.

The corresponding trend of Z_y exhibits much greater zonal variability, with a larger minimum and maximum. Throughout most of the tropics and subtropics, in particular for the SH, the trend of Z_y is strongly negative. Based on the standard interpolation method, Z_y reaches a minimum of –0.95x10^{-5} decade^{-1} near 7°S. The NH is dominated by positive trends, reaching a maximum of +0.5 x10^{-5} decade^{-1} near 12°N. The differences between spatial interpolation methods for Z_y is also larger, with maximum disagreement in the SH subtropics (where the minima based on trend-mapping and the standard method is substantially larger than that based on the binning method). Unlike $\hat{Z}_y$, the trend of Z_y is not symmetric across the equator. One reason why Z_y derived from heights exhibit greater zonal variability is because obtaining Z_y requires computing horizontal derivatives from point values, while $\hat{Z}_y$ is obtained directly at a site from local wind data.

Integration of the trend of Z_y over latitude, gives equivalent trend estimates of $\bar{T}$ relative to an unknown constant offset (i.e. the integration constant) (Fig. 6b). Similar to the trend of $\hat{Z}_y$ in Fig. 6a, the trend of wind-based $\bar{T}$ ($\bar{\hat{T}}_t$) is much more zonally

uniform than the trend of directly measured $\bar{T}$ ($\bar{T}_t$). Furthermore, all three spatial interpolation methods yield similar results for $\bar{\hat{T}}_t$. Both $\bar{T}_t$ and $\bar{\hat{T}}_t$ are relatively similar throughout the SH mid-latitudes/subtropics, with $\bar{T}_t > \bar{\hat{T}}_t$ ($\bar{T}_t$ based on trend-mapping being most similar to the three $\bar{\hat{T}}_t$). North of ~10°S, however, $\bar{T}_t$ and $\bar{\hat{T}}_t$ diverge substantially. Near 5°N, $\bar{T}_t$ decreases to a minimum 2 to 5 times larger than the corresponding minimum of $\bar{\hat{T}}_t$. Over the entire Northern Hemisphere, $\bar{T}_t < \bar{\hat{T}}_t$ based on trend-mapping and the standard interpolation methods.

Although Fig. 6b does not give absolute estimates of the trend in $\bar{T}$, warming/cooling trends of one region, relative to another, can be obtained. Both $\bar{\hat{T}}_t$ and $\bar{T}_t$ show that the equator has cooled relative to both the NH and SH, with a similar rate of cooling for both hemispheres based on $\bar{\hat{T}}_t$. Based on the temperature data, the equator cools at a rate faster than that based on the winds, especially for the SH. If it is assumed that the winds are not affected by discontinuities similar to those that affect the temperature data, this analysis suggests an artificial cooling bias exists in the tropospheric temperature data of the tropical western Pacific. Because only 0000 UTC data is used (which corresponds to daytime in the study area), the artificial cooling indicated here has likely been maximized (e.g. Sherwood et al., 2005), although nighttime data is not exempt from similar cooling biases (Randel and Wu, 2006).

d) HadAT comparisons

Figure 7 compares the decadal trend of $\bar{T}$ and $\bar{\hat{T}}$ using the binning methodology (as shown in Fig. 6b) to the corresponding trend estimates using the raw ($\bar{T}_t^{raw}$) and adjusted ($\bar{T}_t^{adj}$) HadAT. Exact correspondence between the HadAT curves and those based on height or winds should not be expected for several reasons. Tests revealed that the largest source of difference is the inclusion of nighttime (12 Z) data by HadAT. Of the 103 HadAT stations in the study area, 86 included some type of nighttime data (either 12Z monthly mean data or an average of available 00Z and 12Z monthly mean data). An additional reason for differences is that HadAT's "raw" data set has had some adjustments (i.e. there are 11 stations within the study area with adjusted LKS data).

The first thing to note is the difference between $\bar{T}^{raw}$ and $\bar{T}^{adj}$ trends. In the SH (poleward of 10°S), adjustments decrease the trend from approximately 0.2 to 0.15 °C decade^{-1}. North of 10°S, $\bar{T}_t^{raw} < \bar{T}_t^{adj}$, with $\bar{T}_t^{raw}$ assuming negative values (-0.13° C decade^{-1}) near the equator. Both $\bar{T}_t^{raw}$ and $\bar{T}_t^{adj}$ show warming trends north of 10°N, which continue increasing in magnitude to a maximum of 0.3°C decade^{-1} near 35°N. Similar to the comparison between $\bar{T}_t$ and $\bar{\hat{T}}_t$, adjustments to $\bar{T}^{raw}$ suggest an artificial cooling bias in the raw temperature data, which is maximized near the equator.

Because the wind and temperature curves do not represent absolute tropospheric temperature trend estimates (due to the integration constant), only latitudinal changes in the trend of $\bar{T}$ can be compared. Figure 7b shows the corresponding differences between the zonal mean $\bar{T}$ trends in Fig. 7a, with the variability of each difference showing the degree of correspondence between the two zonal mean $\bar{T}$ trends being compared. The difference between $\bar{T}_t$ and the two HadAT trend estimates exhibit large

latitudinal variability. The standard deviation of the difference between $\bar{T}_t$ - $\bar{T}_t^{raw}$ and $\bar{T}_t$ - $\bar{T}_t^{adj}$ is 0.051 °C decade^{-1} and 0.087°C decade^{-1}, respectively. This implies that $\bar{T}$ is more consistent with the unadjusted HadAT data, as would be expected. The difference between $\bar{\hat{T}}_t$ and the adjusted HadAT trend estimate exhibits less zonal variability than the corresponding difference with $\bar{T}_t$. The standard deviation of the difference between $\bar{\hat{T}}_t$ and $\bar{T}_t^{adj}$ is 0.041°C decade^{-1}. Thus the wind-based trend estimates are more consistent with the HadAT adjusted estimates than are the temperature-based estimates. Furthermore, the wind-based estimates and the adjusted HadAT data are more consistent than are the wind-based estimates and the raw HadAT data. This suggests that tropospheric temperature trends based on winds are relatively unaffected by the discontinuities affecting the radiosonde temperature record.

e) MSU satellite comparisons

Figure 8 compares the decadal trend of $\bar{T}$ and $\bar{\hat{T}}$ using the binning method (as shown in Fig. 6b) to the corresponding trend estimates using the satellite Microwave Sounding Unit (MSU) data. MSU trend estimates are shown for two groups—Remote Sensing Systems ($\bar{T}_t^{RSS}$) (Mears et al., 2003) and University of Alabama in Huntsville ($\bar{T}_t^{UAH}$) (Christy et al., 2003). UAH data has been interpolated from the odd grid (i.e. the center of each grid point is 1.25° different from integer multiples of 2.5°) to correspond to the RSS 2.5° x 2.5° grid. The 850-300 hPa layer average satellite temperature has been calculated based on Fu et al. (2004) (FU04 henceforth), which uses a linear combination

of MSU channels 2 and 4 (T2 and T4, respectively) based on tropical average monthly temperature anomaly profiles from radiosonde observations. Based on our time period and station list, the equation for synthetic satellite temperatures is $\bar{T}$ = -0.00066 +1.195*T2-0.1328*T4, which is nearly identical to that found in FU04 for 30°S to 30°N. Figure 8 also shows UAH and RSS $\bar{T}$ trend estimates based on channel 2 brightness temperature alone ($\bar{T}2_t^{UAH}$ and $\bar{T}2_t^{RSS}$). All satellite estimates show relatively little zonal variability, with $\bar{T}_t^{RSS} > \bar{T}_t^{UAH}$ and $\bar{T}2_t^{RSS} > \bar{T}2_t^{UAH}$. For a given satellite analysis, tropospheric trends based on FU04 are larger than those based on channel 2 alone (i.e. $\bar{T}_t^{UAH} > \bar{T}2_t^{UAH}$ and $\bar{T}_t^{RSS} > \bar{T}2_t^{RSS}$). This is consistent with FU04, because channel 2 is partially sensitive to the stratosphere (which has cooled), so subtracting this cooling signal from channel 2, via channel 4, will yield a larger warming trend. However, subtracting the stratosphere's signal from channel 2 seems to simply shift the two curves by an approximately constant offset. The shape of the satellite curves resembles that for $\bar{\hat{T}}_t$. The transition to a more slowly warming equatorial troposphere based on $\bar{\hat{T}}_t$ is also evident in the satellite estimates.

Table 3 lists the corresponding differences between the zonal mean $\bar{T}$ trends in Fig. 8, with the degree of variability of each difference showing the degree of correspondence between the two zonal mean $\bar{T}$ trends being compared. The difference between $\bar{\hat{T}}_t$ and the satellite trend estimates exhibit less variability than the corresponding differences with $\bar{T}_t$. The best correspondence is between $\bar{\hat{T}}_t$ and $\bar{T}_t^{RSS}$, where the standard deviation of the difference is 0.024°C decade^{-1} (a factor of 4.7 less

than that between $\bar{T}_t$ - $\bar{T}_t^{RSS}$). The standard deviation of $\bar{\hat{T}}_t$ - $\bar{T}_t^{UAH}$ is similar at 0.030°C decade^{-1}. As with the height-based trend estimates, the standard deviations of the difference between $\bar{\hat{T}}_t$ and FU04 are slightly smaller than those based on channel 2 alone (except $\bar{\hat{T}}_t$ - $\bar{T}_t^{UAH}$ based on the standard interpolation method). Thus the wind-based trend estimates are more consistent to the satellite based estimates than those based on temperature, with negligible difference between RSS and UAH. Wind-based estimates are slightly more consistent with FU04 than channel 2 alone. These results are consistent with the other two spatial interpolation methods (Table 3).

f) GCM comparisons

The five coupled climate models listed in Table 1 were used to estimate zonal Z_y and $\bar{T}$ trends for the western tropical Pacific, as in Fig 6 based on radiosonde data. The difference between using data from SRES A1B or COMMIT for the last 5 years resulted in negligible differences, so only the COMMIT results are discussed. Figure 9 shows the $\bar{T}$ trends based on ECHAM5/MPI-OM and CCSM3 derived from actual temperatures (for 3 realizations and the mean), as well as height and wind-estimated $\bar{T}$ trends (ensemble mean only). The corresponding wind and height based radiosonde trends from Fig. 6b (binning interpolation method) are also included. Both $\bar{\hat{T}}_t$ and $\bar{T}_t$ based on ECHAM5/MPI-OM (Fig. 9a) show very good agreement with the corresponding trends based on radiosonde winds. As with satellites, little agreement exists between the model estimates and those based on radiosonde heights. The CCSM3 $\bar{T}$ trends (Fig. 9b), however, are quite different than both radiosonde wind and height estimated $\bar{T}$ trends.

For both CCSM3 and ECHAM5/MPI-OM (as well as the other 3 models), there is strong agreement between $\bar{\hat{T}}_t$ and $\bar{T}_t$ derived from each model, which further suggests the utility of Eq. (1).

Based on actual temperatures, the warming trend from two of the three ECHAM5/MPI-OM realizations (as well as the ensemble mean) show minimum warming in the tropics (~0.125° decade^{-1}), increasing by ~0.10° decade^{-1} at the boundary of the domain (32.5° N/S). This is opposite to previous climate model studies that show maximum warming in the tropical middle/upper troposphere (e.g. Karl et al., 2006). As Fig. 9b shows, however, CCSM3 is more consistent with the prior studies. It shows a slightly larger $\bar{T}$ trend near the equator, relative to higher latitudes (in particular in the SH), by 0.05 to 0.1° decade^{-1}. The other 3 models (not shown) have zonally invariant warming. This result suggests global trends are not necessarily indicative of regional trends and radiosonde wind-based $\bar{T}$ trends for the western tropical Pacific are within the range predicted by (some) climate models

5. Conclusions

For the long-term mean (1979-2004), meridional thickness gradients estimated geostrophically from winds agree well with those observed directly from temperature and pressure data. This is true even for tropical latitudes, as shown by radiosonde and climate model data. Seasonal variations are also highly geostrophic, and interannual variations (which are noisier) appear consistent with geostrophy. We were unable to improve on geostrophy with additional (e.g. inertial) terms in the momentum budget. In the GCM runs investigated here, trends in baroclinicity in the study region were practically

indistinguishable whether calculated from wind or from temperature using the TWE.

Time series of the two baroclinicity estimates since 1979 imply that in the western Pacific, tropical thicknesses have decreased relative to those in the subtropics and mid-latitudes of both hemispheres. This result was confirmed using MSU satellite data and is within the range predicted by some climate models. We conclude that the equator to pole temperature gradient and the subtropical jets flanking the Indonesia/warm pool region have weakened.

While the majority of data sources support this weakening, there are significant differences in the degree of warming and in more detailed meridional variations. In general, it appears that the radiosonde (temperature-based) warming estimates are the least reliable, and are dependent of how the data are averaged. There is an evident cooling bias in the tropics, although this appears to be largely removed by the recent HadAT homogenization effort, at least in this region. The sensitivity to averaging, however, makes assessment of any radiosonde dataset difficult. The wind-based baroclinicity estimates are relatively consistent with both the homogenized radiosonde data and especially the satellite data, suggesting that the radiosonde winds are relatively unaffected by heterogeneity issues.

Our independent, wind-based temperature trends agreed slightly better with RSS than with UAH, and slightly better with FU04 than with channel 2 alone. These differences, however, are not large enough to be conclusive and further work is needed.

These results support the conclusion that the wind field has utility in the monitoring of climate change and suggests wind shear-inferred baroclinicity trends are more accurate than those from observed temperature, where inhomogeneities likely cause spurious cooling at tropical stations.

6. Acknowledgments

We thank the anonymous reviewers for their helpful comments on the manuscript, and Michael Joyce, from the Bureau of Meteorology, for kindly supplying information on radiosonde wind measuring techniques.

7. References

Boville, B.A., 1987: The validity of the geostrophic approximation in the winter stratosphere and troposphere. *J. Atmos. Sci*., **44**, 443-457.

Brown, S., D. Parker, C. Folland, and I. Macadam, 2000: Decadal variability in the lower tropospheric lapse rate. *Geophys. Res. Lett.*, **27**, 997-1000.

Christy, J.R., R.W. Spencer, W.B. Norris, W.D. Braswell, D.E. Parker, 2003: Error estimates of Version 5.0 of MSU/AMSU bulk atmospheric temperatures. *J. Atmos. Oceanic Tech*., **20**, 613-629.

Durre, I., R.S. Vose, and D.B. Wuertz, 2006: Overview of the integrated global radiosonde archive. *J. Climate*, **19**, 53-68.

Elliot, W.P., D.J. Gaffen, J.D.W. Kahl, J.K. Angell, 1994: The effect of moisture on later thickness used to monitor global temperatures. *J. Climate*, **7**, 304-308.

Endlich, R., 1961: Computation and uses of gradient winds. *Mon. Wea. Rev*., **89**, 187-191.

Eskridge, R., A. Alduchov, I. Chernykh, Z. Panmao, A. Polansky, and S. Doty, 1995: A comprehensive aerological data set (CARDS): Rough and systematic errors. *Bull. Amer. Meteor. Soc.*, **76**, 1759-1775.

Fankhauser, J.C., 1974: The derivation of consistent fields of wind and geopotential height from mesoscale rawinsonde data. *J. Appl. Meteor*., **13**, 637-646.

FCM-H3, cited 1997: Federal meteorological handbook no. 3: Rawinsonde and pibal observations. [Available online at http://www.ofcm.noaa.gov/fmh3/pdf/00-entire FMH3.pdf]

Free, M., I. Durre, E. Anguilar, D. Seidel, T.C. Peterson, R.E. Eskridge, J.K. Luers, D.

Parker, M. Gordon, J. Lanzante, S. Klein, J. Christy, S. Schroeder, B. Soden, L.M. McMillin, and E. Weatherhead, 2002: Creating climate reference series datasets: CARDS workshop on adjusting radiosonde temperature data for climate monitoring. *Bull. Amer. Meteor. Soc.*, **83**, 891-899.

Free, M., D.J. Seidel, J.K. Angell, J. Lanzante, I. Durre, and T.C. Peterson, 2005: Radiosonde atmospheric temperature products for assessing climate (RATPAC): A new data set of large-area anomaly time series. *J. Geophys. Res.*, **110**, D22101, doi:10.1029/2005JD006169.

Fu, Q., and C.M. Johanson, 2005: Satellite-derived vertical temperature dependence o tropical tropospheric trends. *Geophys. Res. Lett*, **32**, LI0703, doi:10.1029/2004GL022266.

Fu, Q., C.M. Johanson, SG Warren, and DJ Seidel, 2004: Contribution of stratospheric cooling to satellite inferred tropospheric temperature trends. *Nature*, **429**, 55-58.

Gaffen, D., 1994: Temporal inhomogeneities in radiosonde temperature records. *J. Geophys. Res.*, **99**, 3667-3676.

Gaffen, D., B. Santer, J. Boyle, J. Christy, N. Graham, and R. Ross, 2000: Decadal changes in the vertical temperature structure of the tropical troposphere. *Science* **287**, 1239-1241.

Haltiner, G.J. and R.T. Williams, 1980: *Numerical Weather Prediction and Dynamic Meteorology*. John Wiley and Sons, 477 pp.

Isaaks, E.H. and R.M. Srivastava, 1989: *An Introduction to Applied Geostatistics*. Oxford University Press, 561 pp.

Karl, T.R., S.J. Hassol, C.D. Miller, W.L. Murray, editors, 2006: *Temperature Trends in the Lower Atmosphere: Steps for Understanding and Reconciling Differences.* A

Report by the Climate Change Science Program and the Subcommittee on Global Change Research, Washington, DC.

Kinter, J.L., M.J. Fennessy, V. Krishnamurthy and L. Marx, 2004: An evaluation of the apparent interdecadal shift in the tropical divergent circulation in the NCEP-NCAR Reanalysis. *J. Climate*, **17**, 349-361.

Lanzante, J., S. Klein, and D. Seidel, 2003a: Temporal homogenization of radiosonde temperature data. Part I: Methodology. *J. Climate*, **16**, 224-240.

Lanzante, J., S. Klein, and D. Seidel, 2003b: Temporal homogenization of radiosonde temperature data. Part II: Trends, sensitivities, and MSU comparison. *J. Climate*, **16**, 241-262.

Mears, C.A., M.C. Schabel, and F.J. Wentz, 2003: A reanalysis of the MSU channel 2 tropospheric temperature record. *J. Climate*, 16, 3650-3664.

Mori, Y., 1988: A study on climatological aspects of winds in Japan. Part II: Mean fields of the thermal wind. *J. Climate*, **1**, 143-156.

Parker, D.E., and D.I. Cox, 1995: Towards a consistent global climatological rawinsonde data base. *Int. J. Climatol*., **15**, 473-496.

Patoux, J., and R. Brown, 2002: A gradient wind correction for surface pressure fields retrieved from scatterometer winds. *J. Appl. Meteor*., **41**, 133-143.

Pawson, S. and M. Fiorino, 1999: A comparison of reanalyses in the tropical stratosphere. Part 3: Inclusion of the pre-satellite data era. *Climate Dyn*., **15**, 241-250.

Pielke, R.A., T.N. Chase, T.G.F. Kittel, J.A. Knaff and J. Eastman, 2001: Analysis of 200 mbar zonal winds for the period 1958-1997. *J. Geophys. Res*., **106**, (D21) 27,287 27,290.

Randel, W.J., 1987: The evaluation of winds from geopotential height data in the

stratosphere. *J. Atmos. Sci*., **44**, 3097-3120.

Randel, W.J. and F. Wu, 2006: Biases in stratospheric and tropospheric temperature trends derived from historical radiosonde data. *J. Climate*, **19**, 2094-2104.

Raymond, D.J., S.K. Esbensen, C. Paulson, M. Gregg, C.S. Bretherton, W.A. Peterson, R. Cifelli, L.K. Shay, C. Ohlmann, and P. Zuidema, 2004: EPIC2001 and the coupled ocean-atmosphere system of the tropical east Pacific. *Bull. Amer. Meteor. Soc*., **85**, 1341-1354.

Sherwood, S.C., 2000a: Climate signal mapping and an application to atmospheric tides. *Geophys. Res. Lett*., **27**, 3525-3528.

Sherwood, S.C., 2000b: Climate signals from station arrays with missing data, and an application to winds. *J. Geophys. Res*. **105**, (D24), 29489-29500).

Sherwood, S.C., J.R. Lanzante, and C.L. Meyer, 2005: Radiosonde daytime biases and late 20th century warming. *Science*, **309**, 1556-1559.

Tett, S.F.B., G.S. Jones, P.A. Stott, D.C. Hill, J.F.B Mitchell, M.R. Allen, W.J. Ingram, T.C. Johns, C.E. Johnson, A. Jones, D.L. Roberts, D.M.H. Sexton, and M.J. Woodage, 2002: Estimation of natural and anthropogenic contributions to twentieth century temperature change. *J. Geophys. Res.*, **107**, (D16), 4306, doi:10.1029/2000JD000028.

Thorne, P.W., D.E. Parker, S.F.B. Tett, P.D. Jones, M. McCarthy, H. Coleman, and P. Brohan, 2005: Revisiting radiosonde upper air temperatures from 1958 to 2002. *J. Geophys. Res.*, **110**, D18105, doi:10.1029/2004JD005753.

Trenberth, K.E. and L. Smith, 2005: The mass of the atmosphere: A constraint on global analyses. *J. Climate*, **18**, 864-875.

Trenberth, K.E., J. Fasullo, and L. Smith, 2005: Trends and variability in column

integrated atmospheric water vapor. *Climate Dyn*., **24**, 741-758.

van Loon, H., J.J. Taljaard, T. Sasamori, J. London, D.V. Hoyt, K. Labitzke, and C.W. Newton, 1972: *Meteorology of the Southern Hemisphere. Meteor. Monogr*., No. 13, Amer. Meteor. Soc. 263 pp.

Vinnikov, K.Y., N.C. Grody, A. Robock, R.J. Stouffer, P.D. Jones, and M.D. Goldberg, 2006: Temperature trends at the surface and in the troposphere. *J. Geophys. Res.*, **111**, doi:10.1029/2005jd006392, 2006.

Wu H-W and K.H. Jehn, 1972: Geostrophic wind deviation in the upper troposphere an lower stratosphere in the El Paso-White Sands area. *Mon. Wea. Rev*., **100**, 159 -167.

Wentz, F.J. and M. Schabel, 2000: Precise climate monitoring using complementary satellite data sets. *Nature*, **403**, 414-416.

Wilks, D.S., 1995: *Statistical Methods in the Atmospheric Sciences*. Academic Press, 467 pp.

Figure Captions

Figure 1. Map of the study area, bounded by the rectangle defined by 32.5°S ϕ 32.5°N and 95°E λ 175°E, and location of the 59 radiosondes (crosses) used in the analysis.

Figure 2. Top Panel: Long-term mean wind-estimated ($\hat{Z}_y$) and height-estimated (Z_y) meridional thickness gradients for each of the 59 radiosondes. Error bars for $\hat{Z}_y$ are estimated according to $|-\frac{f}{g}\frac{2s_S'}{\sqrt{n-1}}|$; error bars for Z_y are estimated as $\frac{s_Z}{r_y}$. Bottom Panel: As in the top panel, but based on the ensemble mean of ECHAM5/MPI-OM using the 20CEN and COMMIT experiments for grid points between 10°N and 10°S. 10^{-5} is approximately equivalent to 1 m height change per degree latitude.

Figure 3. Observed (black) and wind-estimated (gray) long-term (annual) mean thickness gradient shown a. spatially; and b. by zonal mean. Negative contours are dashed in a. Error bars in b. are analogous to those in Figure 2, except for $\hat{Z}_y$, which are estimated as $|-\frac{fs_S}{g}|$.

Figure 4. As in Figure 3, but for the long-term seasonal (DJF-JJA) difference.

Figure 5. Time series of annual-area averaged Z_y (solid black) $\hat{Z}_y$ (solid gray), and Z_y - $\hat{Z}_y$ (black dashed) for eight latitude bands. The corresponding linear trend line is also shown.

Figure 6. Top Panel: Latitude versus the linear least-squares trend of the zonal-annual mean meridional thickness gradient calculated from temperature (black) and wind estimates (gray). Bottom Panel: The corresponding decadal (relative) trend in vertically-averaged tropospheric temperature based on temperature ($\bar{T}_t$) and wind ($\bar{\hat{T}}_t$). Three spatial gridding methods are shown, 1. standard (solid); 2. trend-mapping (dash); and 3. binning (dash-dot). Error bars indicate the 1-σ uncertainty in the estimated trend in Z_y. In integrating (a) to get (b), the integration constant is arbitrarily set to zero at the southernmost location.

Figure 7. Top Panel: Comparison of the decadal (relative) trend of $\bar{T}$ from Fig. 6b (black) based on temperature (dashed) and wind estimates (solid) using the binning interpolation method versus the corresponding trend estimates based on HadAT (gray) raw (dashed) and adjusted (solid) data. Bottom Panel: The corresponding differences between the zonal mean $\bar{T}$ trends in the top panel, $\bar{\hat{T}}_t$ - $\bar{T}_t^{adj}$ (black solid); $\bar{\hat{T}}_t$ - $\bar{T}_t^{raw}$ (black dashed); $\bar{T}_t$ - $\bar{T}_t^{raw}$ (gray dashed); and $\bar{T}_t$ - $\bar{T}_t^{adj}$ (gray solid).

Figure 8. Comparison of the decadal (relative) trend of $\bar{T}$ based on temperature (gray) and wind estimates (black) using the binning interpolation method (dash-dot) versus the corresponding trend estimates based on UAH (black) and RSS (gray) data using Fu et al.

(2004) methodology (solid) and channel 2 alone (dashed). The (zonal) average 1-σ uncertainty in the satellite trends using FU04 are 0.068°C decade^{-1} (RSS) and 0.066°C decade^{-1} (UAH); and 0.058°C decade^{-1} (RSS) and 0.055°C decade^{-1} (UAH) using channel 2.

Figure 9. Comparison of the decadal (relative) trend of $\bar{T}$ based on heights (black) and winds (gray) using the binning interpolation method (dashed) versus the corresponding trend estimates based on the ensemble mean of the ECHAM5/MPI-OM model (top panel) and the CCSM3 (bottom panel) using the 20CEN and COMMIT experiments (solid). Each model's $\bar{T}$ trend based on actual temperature is also shown for 3 realizations (dotted; dash dot-dot; long dash), as well as the ensemble mean (dash-dot).

Figures

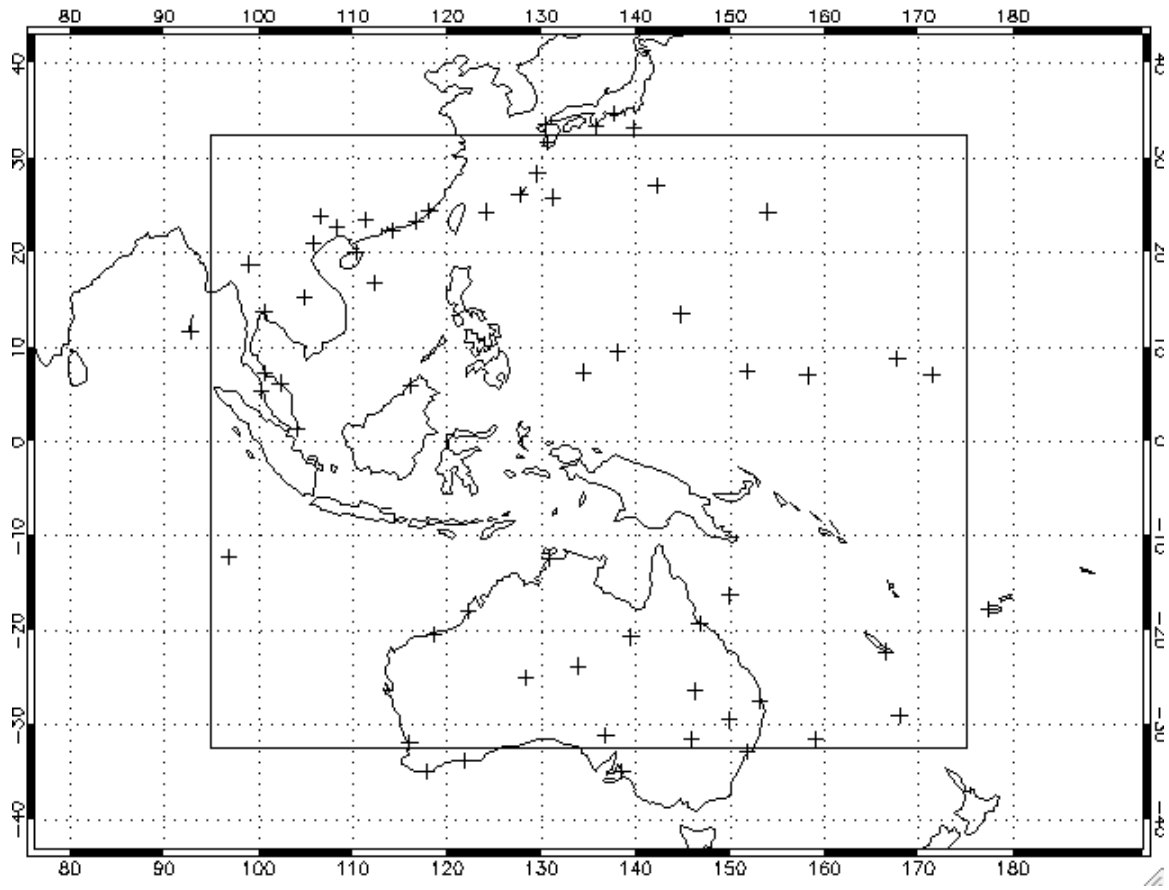

Figure 1. Map of the study area, bounded by the rectangle defined by 32.5°S ϕ 32.5°N and 95°E λ 175°E, and location of the 59 radiosondes (crosses) used in the analysis.

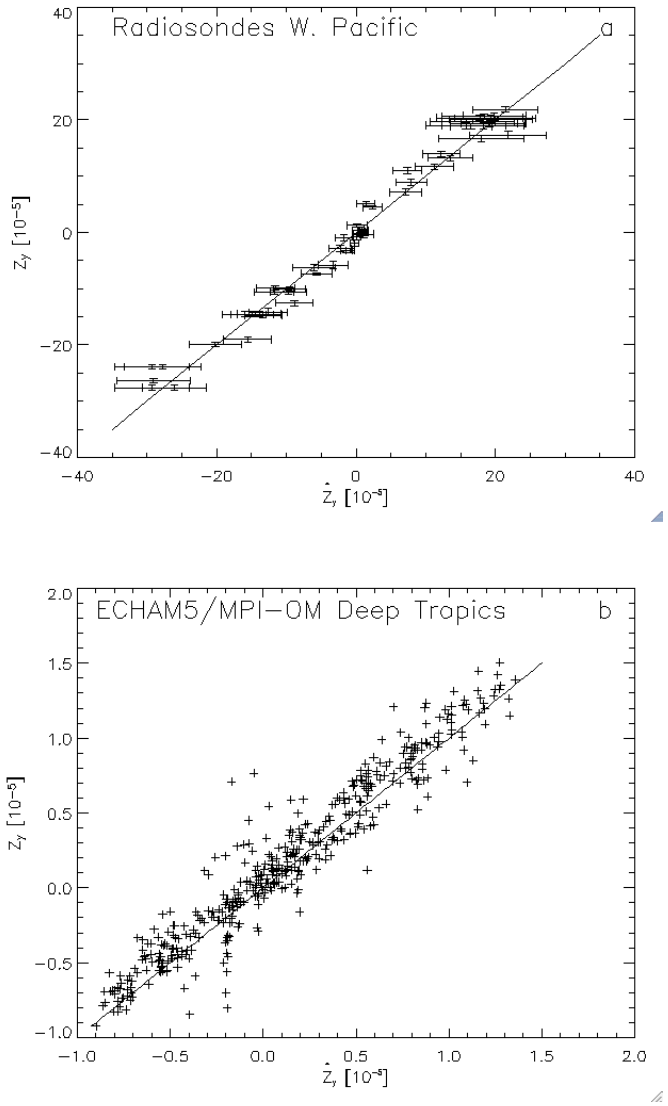

Figure 2. Top Panel: Long-term mean wind-estimated ($\hat{Z}_y$) and height-estimated (Z_y) meridional thickness gradients for each of the 59 radiosondes. Error bars for $\hat{Z}_y$ are estimated according to $|-\frac{f}{g}\frac{2s_S'}{\sqrt{n-1}}|$; error bars for Z_y are estimated as $\frac{s_Z}{r_y}$. Bottom Panel: As in the top panel, but based on the ensemble mean of ECHAM5/MPI-OM using the 20CEN and COMMIT experiments for grid points between 10°N and 10°S. 10^{-5} is approximately equivalent to 1 m height change per degree latitude.

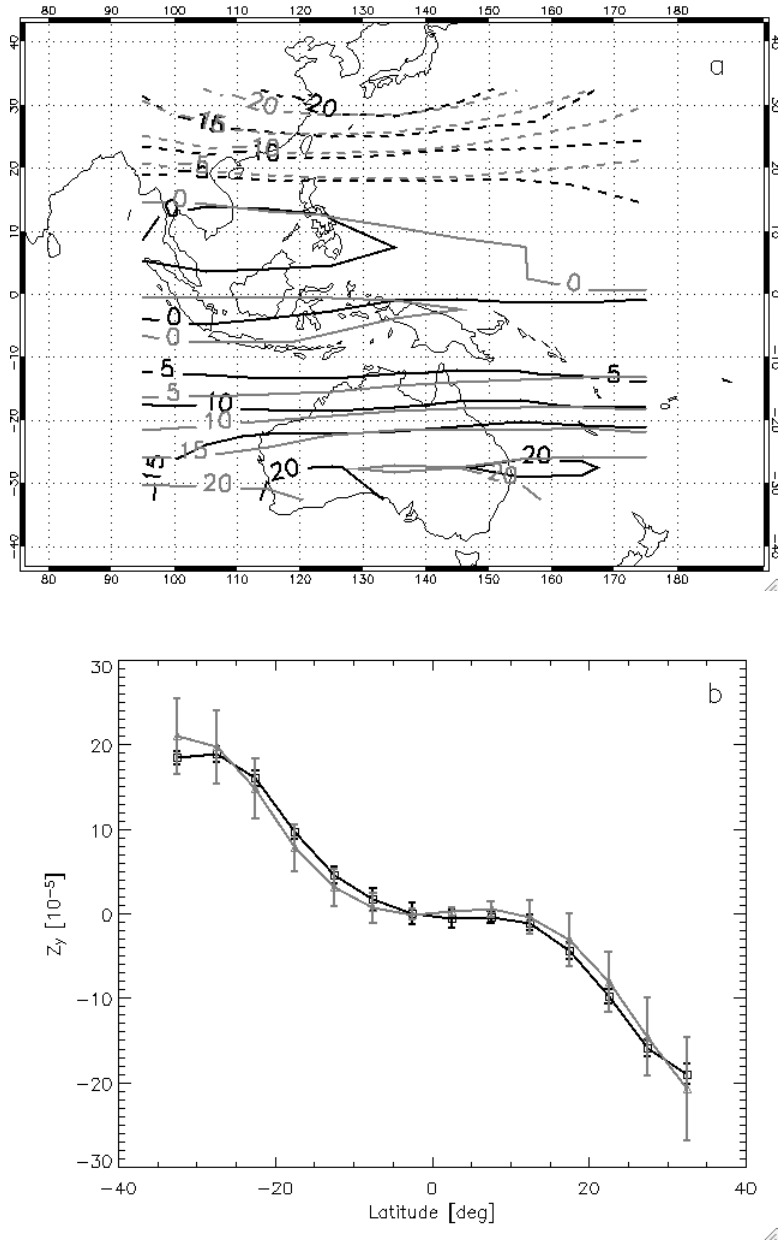

Figure 3. Observed (black) and wind-estimated (gray) long-term (annual) mean thickness gradient shown a. spatially; and b. by zonal mean. Negative contours are dashed in a. Error bars in b. are analogous to those in Figure 2, except for $\hat{Z}_y$, which are estimated as

$$|-\frac{fs_S}{g}| \ .$$

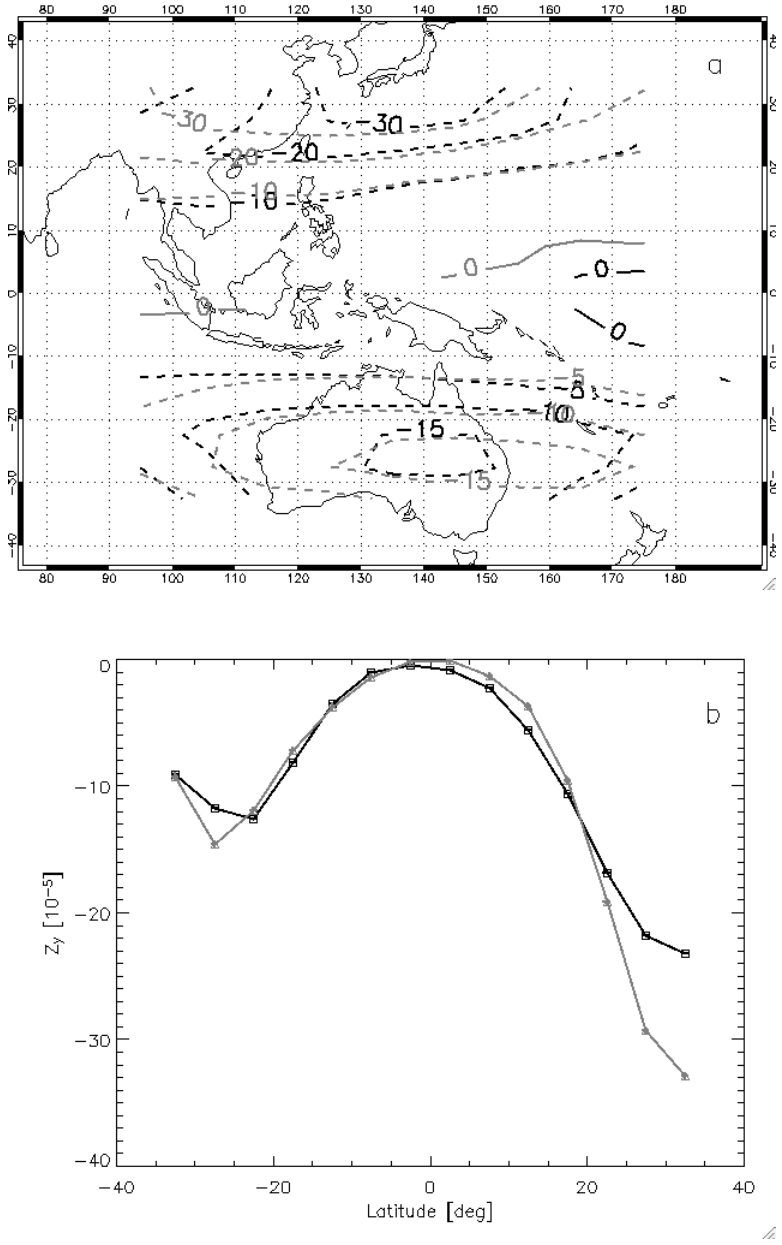

Figure 4. As in Figure 3, but for the long-term seasonal (DJF-JJA) difference.

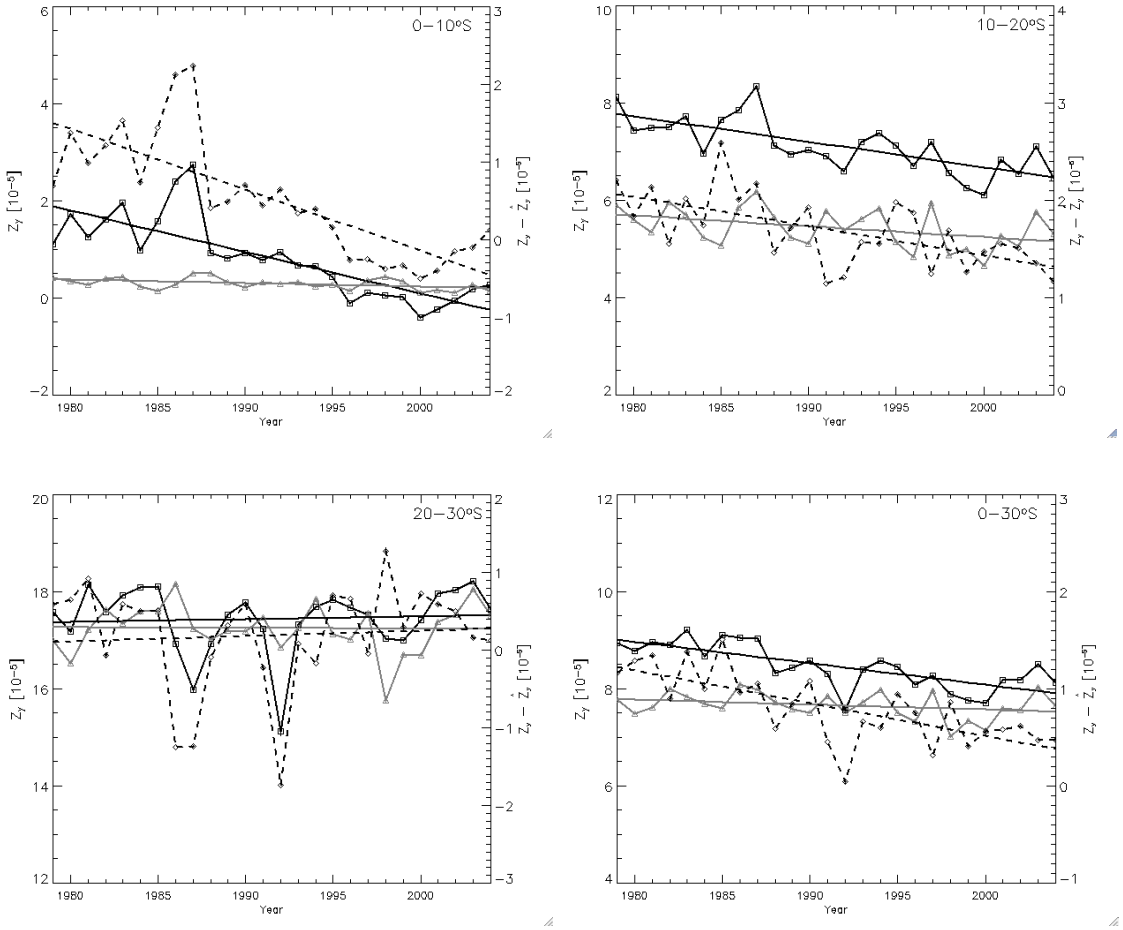

Figure 5. Time series of annual-area averaged Z_y (solid black) $\hat{Z}_y$ (solid gray), and Z_y - $\hat{Z}_y$ (black dashed) for eight latitude bands. The corresponding linear trend line is also shown.

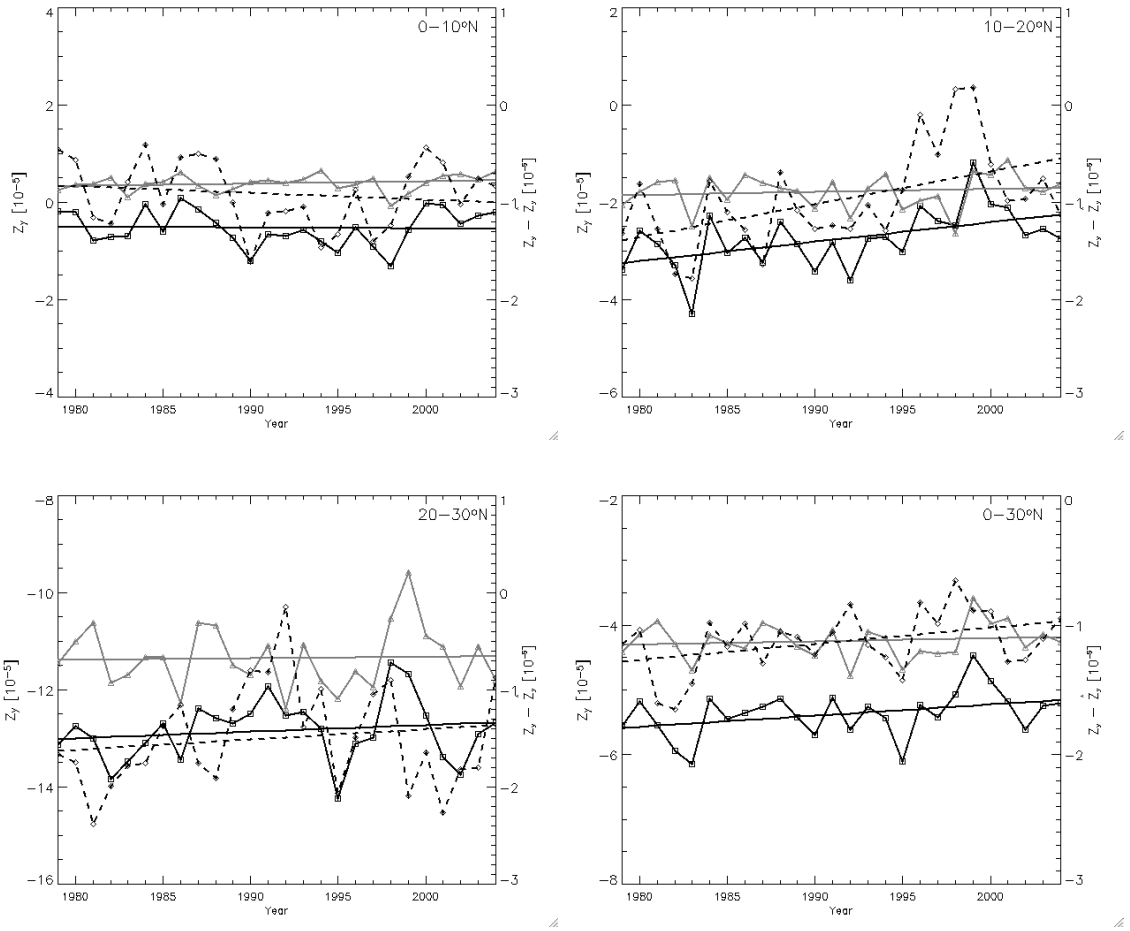

Figure 5. (continued)

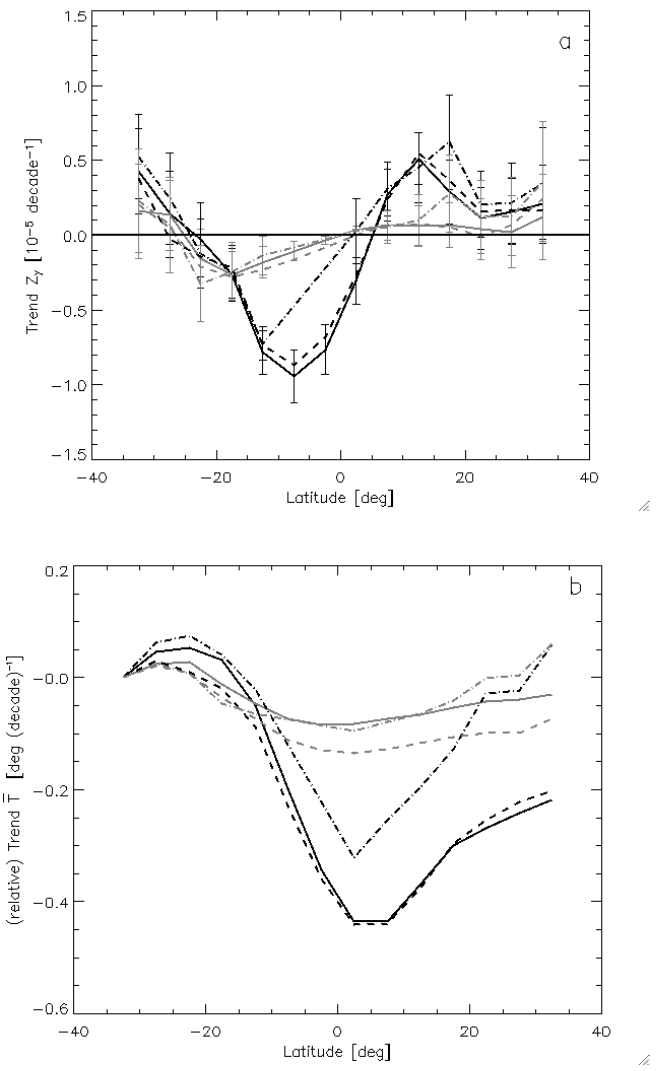

Figure 6. Top Panel: Latitude versus the linear least-squares trend of the zonal-annual mean meridional thickness gradient calculated from temperature (black) and wind estimates (gray). Bottom Panel: The corresponding decadal (relative) trend in vertically-averaged tropospheric temperature based on temperature ($\bar{T}_t$) and wind ($\bar{\hat{T}}_t$). Three spatial gridding methods are shown, 1. standard (solid); 2. trend-mapping (dash); and 3. binning (dash-dot). Error bars indicate the 1-σ uncertainty in the estimated trend in Z_y. In integrating (a) to get (b), the integration constant is arbitrarily set to zero at the southernmost location.

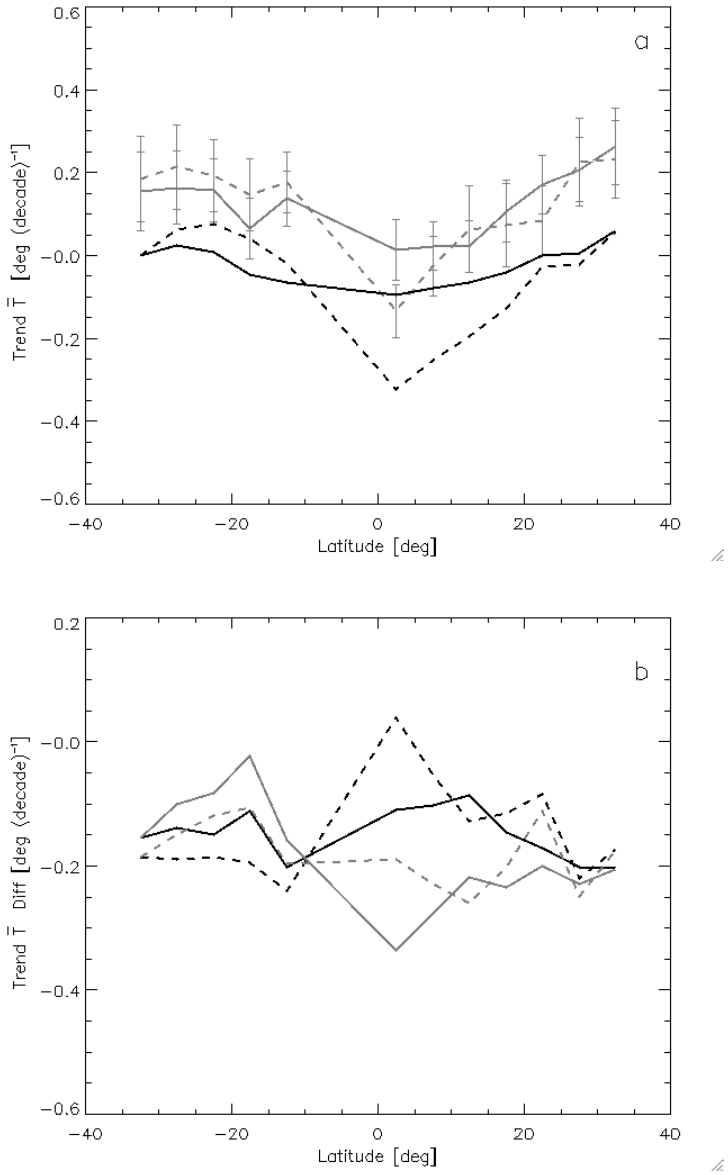

Figure 7. Top Panel: Comparison of the decadal (relative) trend of $\bar{T}$ from Fig. 6b (black) based on temperature (dashed) and wind estimates (solid) using the binning interpolation method versus the corresponding trend estimates based on HadAT (gray) raw (dashed) and adjusted (solid) data. Bottom Panel: The corresponding differences between the zonal mean $\bar{T}$ trends in the top panel, $\bar{\hat{T}}_t$ - $\bar{T}_t^{adj}$ (black solid); $\bar{\hat{T}}_t$ - $\bar{T}_t^{raw}$ (black dashed); $\bar{T}_t$ - $\bar{T}_t^{raw}$ (gray dashed); and $\bar{T}_t$ - $\bar{T}_t^{adj}$ (gray solid).

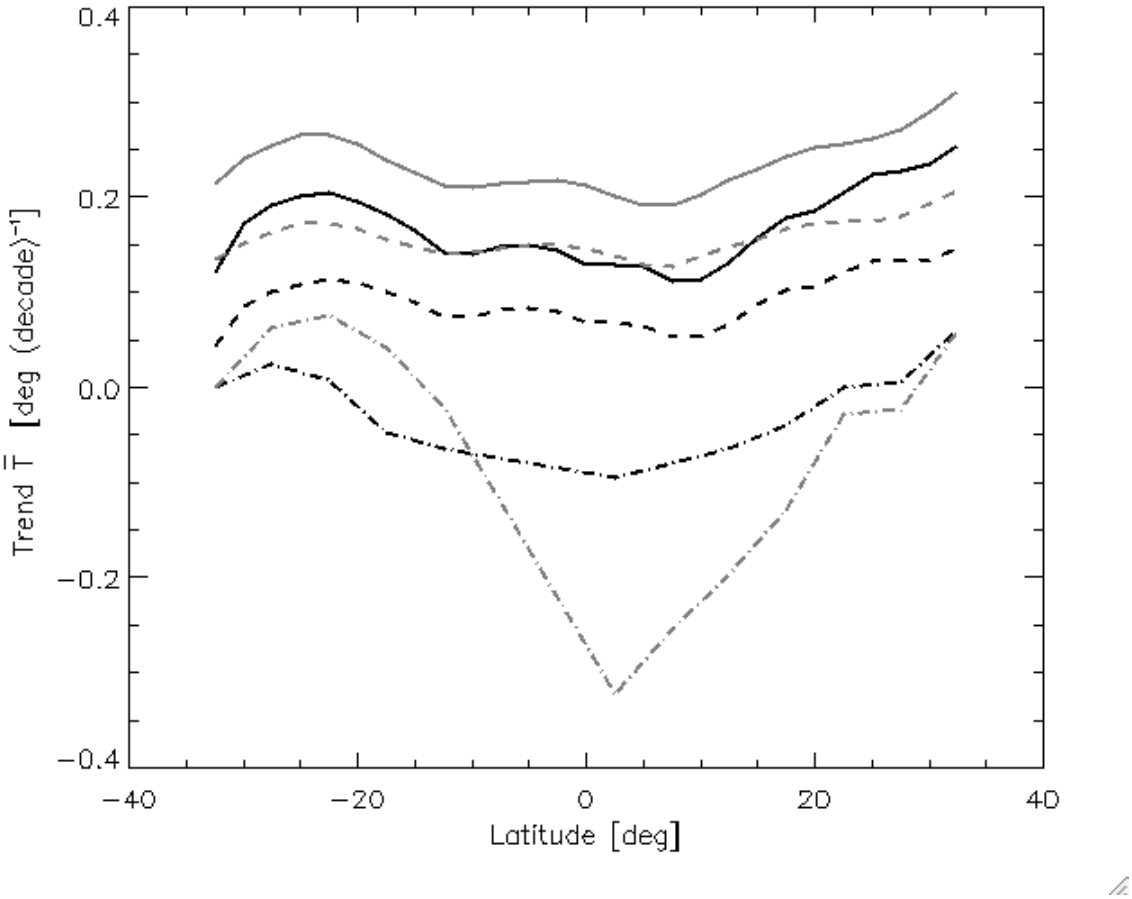

Figure 8. Comparison of the decadal (relative) trend of $\bar{T}$ based on temperature (gray) and wind estimates (black) using the binning interpolation method (dash-dot) versus the corresponding trend estimates based on UAH (black) and RSS (gray) data using Fu et al. (2004) methodology (solid) and channel 2 alone (dashed). The (zonal) average 1-σ uncertainty in the satellite trends using FU04 are 0.068°C decade^{-1} (RSS) and 0.066°C decade^{-1} (UAH); and 0.058°C decade^{-1} (RSS) and 0.055°C decade^{-1} (UAH) using channel 2.

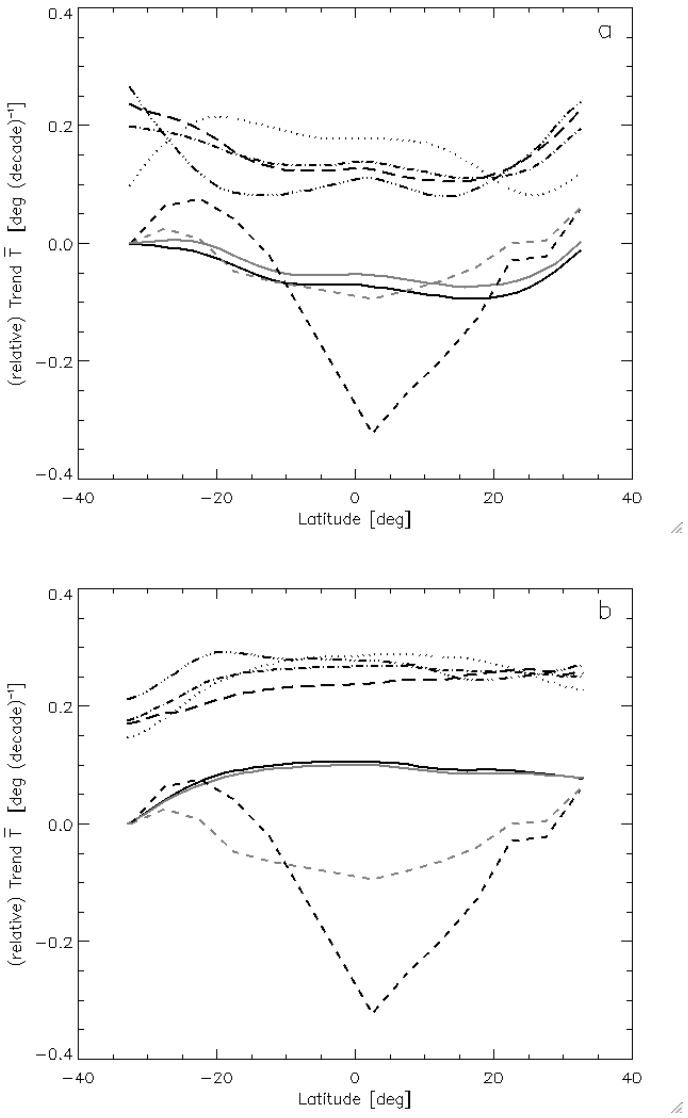

Figure 9. Comparison of the decadal (relative) trend of $\bar{T}$ based on heights (black) and winds (gray) using the binning interpolation method (dashed) versus the corresponding trend estimates based on the ensemble mean of the ECHAM5/MPI-OM model (top panel) and the CCSM3 (bottom panel) using the 20CEN and COMMIT experiments (solid). Each model's $\bar{T}$ trend based on actual temperature is also shown for 3 realizations (dotted; dash dot-dot; long dash), as well as the ensemble mean (dash-dot).

Tables

Table 1. Acronyms of coupled climate models from the IPCC Fourth Assessment Report

used in this study. The ensemble size, ES, is the number of independent realizations of the 20th Century Climate Change experiment (used from 1979-1999), along with the SRES A1B or Committed Climate Change experiments (used from 2000-2004).

Model Acronym	Country	Institution	ES
CCCma-CGCM3.1(T47)	Canada	Canadian Center for Climate Modeling and Analysis	5
CCSM3	United States	National Center for Atmospheric Research	5
ECHAM5/MPI-OM	Germany	Max-Planck Institute for Meteorology	3
FGOALS-g1.0	China	Institute for Atmospheric Physics	3
PCM	United States	National Center for Atmospheric Research	3

Table 2. The 1979-2004 Z_y trends (x10^{-5} $decade^{-1}$) and significance by latitude band. The correlation, ρ, between Z_y and $\hat{Z}_y$ is also shown in the last column. Trend and correlation significance is denoted by bold (90%); * (95%); ** (99%).

Latitude Band	Z_y	$\hat{Z}_y$	$Z_y - \hat{Z}_y$	ρ
0-10° N	-0.002	0.004	-0.007	**0.36**

10-20° N	**0.040****	0.006	**0.034****	**0.56****
20-30° N	0.014	0.003	0.011	**0.65****
0-30° N	**0.017**	0.005	**0.012***	**0.75****
0-10° S	**-0.085****	**-0.007***	**-0.078****	**0.50****
10-20° S	**-0.052****	**-0.022****	**-0.032****	**0.74****
20-30° S	0.005	-0.001	0.007	**0.35**
0-30° S	**-0.044****	-0.010	**-0.034****	**0.61****

Table 3. Standard deviation (°C decade^{-1}) of the difference between wind- or height-based zonal mean $\bar{T}$ trends and UAH or RSS satellite zonal mean $\bar{T}$ trends. The two satellites are shown for channel 2 alone, and the methodology of Fu et al. (2004). Trends of $\bar{T}$ and $\bar{\hat{T}}$ are shown for the three spatial interpolation methods.

		Standard		Trend-Mapping		Binning	
		$\bar{T}$	$\bar{\hat{T}}$	$\bar{T}$	$\bar{\hat{T}}$	$\bar{T}$	$\bar{\hat{T}}$
UAH	Fu	0.172	0.042	0.158	0.057	0.108	0.030
	ch 2	0.177	0.040	0.164	0.058	0.118	0.034
RSS	Fu	0.171	0.035	0.158	0.052	0.112	0.024
	ch 2	0.177	0.036	0.165	0.054	0.121	0.032

Appendix

Radiosondes used in this study.

WMO No.	Station	Location	Lat	Lon
43333	Port Blair	India	11.67	92.72
45004	King's Park	China	22.32	114.17
47678	Hachijo Jima	Japan	33.12	139.78
47681	Hamamatsu AFB	Japan	34.75	137.70
47778	Shionomisaki	Japan	33.45	135.77
47807	Fukuoka	Japan	33.58	130.38
47827	Kagoshima	Japan	31.63	130.60
47909	Naze	Japan	28.38	129.55
47918	Ishigakijima	Japan	24.33	124.17
47936	Naha	Japan	26.20	127.68
47945	Minamidaito Jima	Japan	25.83	131.23
47971	Chichi Jima	Japan	27.08	142.18
47991	Marcus Is.	Japan	24.30	153.97
48327	Chiang Mai	Thailand	18.78	98.98
48407	Ubon Ratchathani	Thailand	15.25	104.87
48455	Bangkok	Thailand	13.73	100.57
48568	Songkhla	Thailand	7.20	100.60
48601	Penang/Bayan Lepas	Malaysia	5.30	100.27
48615	Kota Bharu	Malaysia	6.17	102.28
48698	Singapore/Changi	Singapore	1.37	103.98
48820	Hanoi	Vietnam	21.02	105.80
59134	Xiamen (Amoy)	China	24.45	118.07
59211	Bose	China	23.90	106.60
59265	Wuzhou	China	23.48	111.30
59316	Shantou	China	23.35	116.68
59431	Nanning	China	22.63	108.22
59758	Haikou	China	20.03	110.35
59981	Xisha Dao	China	16.83	112.33
91212	Agana	N. Mariana Is.	13.48	144.8
91334	Chuuk	Fed. St. Micronesia	7.47	151.85
91348	Ponape	Fed. St. Micronesia	6.97	158.22
91366	Kwajalein Atoll	Marshall Is.	8.73	167.73
91376	Majuro Atoll	Marshall Is.	7.08	171.38
91408	Koror	Belau	7.33	134.48
91413	Yap	Fed. St. Micronesia	9.48	138.08
91592	Noumea	New Caledonia	-22.27	166.45
91680	Nadi Airport	Fiji	-17.75	177.45
94120	Darwin	Australia	-12.43	130.87
94203	Broome Airport	Australia	-17.95	122.23
94294	Townsville	Australia	-19.25	146.77

94299	Willis Island	Coral Sea Is.	-16.30	149.98
94312	Port Hedland AMO	Australia	-20.37	118.63
94326	Alice Springs	Australia	-23.80	133.90
94332	Mount Isa AMO	Australia	-20.68	139.48
94461	Giles	Australia	-25.03	128.28
94510	Charleville	Australia	-26.42	146.28
94578	Brisbane	Australia	-27.43	153.08
94610	Perth Airport	Australia	-31.93	115.97
94638	Esperance	Australia	-33.83	121.88
94659	Woomera	Australia	-31.15	136.80
94672	Adelaide Airport	Australia	-34.95	138.53
94711	Cobar MO	Australia	-31.48	145.83
94776	Williamtown	Australia	-32.82	151.83
94802	Albany	Australia	-34.95	117.80
94995	Lord Howe Island	Australia	-31.53	159.07
94996	Norfolk Island	Norfolk Is.	-29.03	167.93
95527	Moree	Australia	-29.48	149.85
96471	Kota Kinabalu	Malaysia	5.95	116.05
96996	Cocos Island	Cocos Islands	-12.18	96.83